Applied Catalysis B: Environmental 236 (2018) 212–221

Contents lists available at ScienceDirect

Applied Catalysis B: Environmental

journal homepage: www.elsevier.com/locate/apcatb

Synthesis of nitrogen and sulfur co-doped reduced graphene oxide as efficient metal-free cocatalyst for the photo-activity enhancement of CdS

Weiwei Han[a], Lulu Chen[b], Weiyu Song[b,*], Shaobin Wang[c], Xiaobin Fan[a], Yang Li[a], Fengbao Zhang[a], Guoliang Zhang[a], Wenchao Peng[a,*]

[a] School of Chemical Engineering and Technology, Tianjin University, Tianjin 300050, China
[b] State Key Laboratory of Heavy Oil Processing, College of Science, China University of Petroleum, Beijing, Beijing 102249, China
[c] Department of Chemical Engineering, Curtin University, GPO Box U1987, Perth WA 6845, Australia

ARTICLE INFO

Keywords:
Nitrogen and sulfur co-doped rGO
Photocatalysis
Hydrogen generation
4-nitrophenol reduction
DFT calculations

ABSTRACT

Nitrogen and sulfur co-doped reduced graphene oxide (NS-rGO) was synthesized using a facile low temperature calcination method, which was then used as support and cocatalyst for the anchor of CdS. The obtained CdS/NS-rGO nanocomposites exhibit ultra-high photocatalytic activity for hydrogen evolution and 4-nitrophenol (4-NP) reduction under visible light ($\lambda \geq 420$ nm). Their activity could also be adjusted by changing the doping amount of S and N, or by changing the ratios between CdS and NS-rGO. The optimum percentage of NS-rGO is 5 wt%, at which CdS/NS-rGO photocatalyst could achieve the highest H_2 evolution rate of 1701 μmol h^{-1} g^{-1}. Moreover, the reduction from 4-NP to 4-aminophenol (4-AP) could be completed within only 6 min over this optimized composite. NS-rGO here could provide more active sites as well as tune the band gap structure to increase the photo-activity. The density functional theory (DFT) calculations reveal that NS-rGO has a small Gibbs free energy for H* adsorption (ΔG_H), which could increase the utilization efficency of photo-generated electrons for H_2 generation. NS-rGO is therefore an idea alternate cocatalyst of noble metals for new photocatalysts development.

1. Introduction

Fossil fuel depletion and environment pollution are two most serious problems in the world nowadays. Hydrogen, as a kind of environmental friendly clean energy, is considered to be the most potential alternative energy [1]. Among the present hydrogen production methods, photocatalytic water splitting by using semiconductors as photocatalysts and sustainable solar light as energy source is the ideal way to produce hydrogen on a large scale [2,3]. In addition, semiconductor based photocatalytic technology is also regarded as a powerful tool for environmental remediation [4]. However, the photo-generated hole and electron pairs can recombine easily on the pure semiconductors, leading to the limited activity from real application. To develop highly efficient and stable photocatalysts is still a big challenge in the photocatalysis field.

The commercial photocatalysts, such as TiO_2, ZnO [5–8], are only active under UV-light due to the wide band gaps, which cannot make full use of sunlight energy [9]. As a typical II—VI semiconductor material, CdS has been a popular visible light active photocatalyst for a long time because of its narrow bandgap (2.42 eV) and excellent visible light absorption performance [10,11]. However, the photo-activity of CdS is still limited due to fast recombination of electron-hole pairs and severe photo-corrosion [12]. A number of strategies, such as morphologies variation, cocatalysts loading, and elements doping, have been used to improve the photocatalytic activity and stability of CdS [13–16].

Graphene (GR), a sp^2-hybridized two-dimensional (2D) carbon nanomaterial, possesses high charge mobility (ca. 10,000 cm^2 V^{-1} s^{-1}) and very large theoretical surface area (2630 m^2 g^{-1}) [17]. In recent years, the reduced graphene oxide (rGO) have been widely applied in the photocatalysis field [18–21]. RGO here can be used as cocatalyst and support for semiconductors, and the presence of rGO could suppress the aggregation of semiconductor particles and facilitate charge carriers transport, thus dramatically improving the photocatalytic performance [22]. Doping with heteroatoms (B, N, S, etc.) could improve electronic properties of rGO and obtain better co-catalytic activities [23–25]. Han et al. reported that CdS nanowires supported on the surface of N-doped rGO exhibited higher photocatalytic activity than that of blank CdS nanowires (CdS NWs) and CdS NWs-rGO nanocomposites for photocatalytic selective reduction of nitro aromatic compounds in water [26]. To modify the N-doped rGO further with second heteroatom (B, P, S), more efficient electrocatalysts could be obtained via a synergistic

* Corresponding authors.
E-mail addresses: songwy@cup.edu.cn (W. Song), wenchao.peng@tju.edu.cn (W. Peng).

https://doi.org/10.1016/j.apcatb.2018.05.021
Received 18 January 2018; Received in revised form 2 May 2018; Accepted 7 May 2018
Available online 08 May 2018
0926-3373/

effect [25,27,28]. Specially, the N,S-rGO has the best activity than other dual heteroatom-doped carbon materials both for hydrogen evolution and permonosulfate activation, attributing to the re-distributed surface charge and electrostatic potential of graphene [29,30]. Photocatalytic reactions usually include a charge utilization process, the N,S-rGO should be therefore an effective cocatalyst due to its enhanced electrocatalytic activity [31].

In this study, we synthesized a series of CdS based photocatalysts with N, S co-doped reduced graphene oxide (NS-rGO) as cocatalyst, and the synergetic effect of NS-rGO is investigated both experimentally and theoretically. The superior photocatalytic behavior of the CdS/NS-rGO nanocomposites was tested toward H_2 generation and 4-nitrophenol (4-NP) reduction under visible light irradiation ($\lambda \geq 420$ nm). Significantly, the photocatalytic activity of the composites was related to the percentage of the NS-rGO as well as the doping ratio between nitrogen and sulfur on rGO. In addition, density functional theory (DFT) were also used to calculate the Gibbs free energy for H* adsorption of the doped rGO. Based on the experiment and calculations results, the photocatalytic activity enhancement mechanism was concluded.

2. Experimental section

2.1. Catalyst synthesis

Cadmium acetate dehydrate ($Cd(CH_3COO)_2{\cdot}2H_2O$), sodium sulfide ($Na_2S$), diphenyl disulfide (DDS), ammonium nitrate (NH_4NO_3), ammonium formate ($HCOONH_4$) were purchased from Aladdin Chemistry Co., Ltd., Shanghai, China. Graphite powder (> 99.99%) was purchased from HWRK Chem Co., Ltd., Beijing, China. Lactic acid was purchased from J&K Scientific Ltd., Beijing, China. 4-nitrophenol (4-NP) was obtained from Innochem Science&Technology Co., Ltd., Beijing, China. All of the reagents were used as received without further purification. The deionized water was used in all experiments.

Synthesis of GO and NS-rGO. Graphene oxide (GO) was prepared using the modified Hummers' method [32]. N,S co-doped reduced graphene oxide (NS-rGO) was synthesized using our previous method. [29] Typically, 1 g freeze-dried GO was uniformly dispersed in 100 ml of ethanol. 1 g NH_4NO_3 and 0.3 g DDS (unless otherwise noted) were then added into the suspension. Keep heating under stirring to remove the solvent at 50 °C. The mixture was then put into the muffle furnace for calcination at 350 °C for 1 h to obtain the final NS-rGO sample. Similarly, rGO, N-rGO and S-rGO were prepared with the introducing of corresponding dopant precursor. Subsequently, the addition amount of DDS was adjusted to 0.05, 0.1, 0.3 and 0.5 g with the same NH_4NO_3 addition to prepare different NS-rGO samples.

Synthesis of CdS/NS-rGO nanocomposites. The fabrication process of CdS/NS-rGO nanocomposites is described in Fig. 1. 4 mmol Cd $(CH_3COO)_2{\cdot}2H_2O$ was first dissolved in 40 ml DI water, 20 ml Na_2S (0.2 M) solution was then added dropwise to the solution under vigorous stirring. Keep stirring for 24 h. After that, the orange CdS precipitate was separated by centrifugation and washed three times with DI water and ethanol to remove the non-reacted reactants. 150 mg pre-prepared CdS was mixed with NS-rGO in 50 ml ethanol, and the solvent was then evaporated at 60 °C. Afterwards, the sample was annealed in argon flow at 400 °C for 2 h. In this way, we obtained a series of CdS/x% NS-rGO by adjusting the mass ratios of NS-rGO to CdS (x = 0, 1, 3, 5, 6 and 10). For comparison, CdS/GO, CdS/rGO, CdS/N-rGO, CdS/S-rGO and CdS/NS-rGO with different doping ratios of nitrogen to sulfur atoms were all prepared in the same method with the addition of 5 wt% to CdS.

2.2. Characterization

The samples were characterized by X-ray diffraction (XRD, Bruker-Nonius D8 Focus diffractometer), scanning electron microscopy (SEM, Hitachi S-4800), transmission electron microscopy (TEM, Philips Tecnai G2 F20), Fourier transform infrared spectroscopy (FT-IR, Thermo-Nicolet 380), Raman spectrometer (Renishaw InVia reflex, 633 nm laser), X-ray photoelectron spectroscopy (XPS) and XPS valence band (VB-XPS) (PerkinElmer PHI1600 spectrometer). UV–vis diffused reflectance spectra was carried out using a UV–vis spectrophotometer (PerkinElmer Lambda 35). The specific surface area (SSA) and pore size distribution was determined on a Bjbuilder SSA-7000. The photoluminescence (PL) spectra and the time-resolved fluorescence spectra were determined on a fluorophotometer (HORIBA Jobin Yvon Fluorolog-3).

2.3. Computational methods

To understand the effect of N-doped, S-doped and N, S-co-doped graphene on hydrogen evolution reaction, we adopted density functional theory (DFT) calculations to investigate the chemisorption of H atom. All the calculations were performed with the Perdew-Burke-Ernzerhof (PBE) [33] as implemented in the Vienna Ab Initio Simulation Package (VASP) [34–36]. The projector augmented wave (PAW) method was used to describe the interaction between the ions and the electrons with frozen-core approximation [37–39]. The plane-wave basis set within a kinetic cut-off energy of 400 eV and the k-points meshes of 1 × 1 ×1 was used for the Brillouim zone integration. Stationary points were identified by the conjugate gradient method was identified until the force acting on each atom smaller than 0.05 eV/Å. The convergence tolerance of the energy was set to be 10^{-4} eV. In our

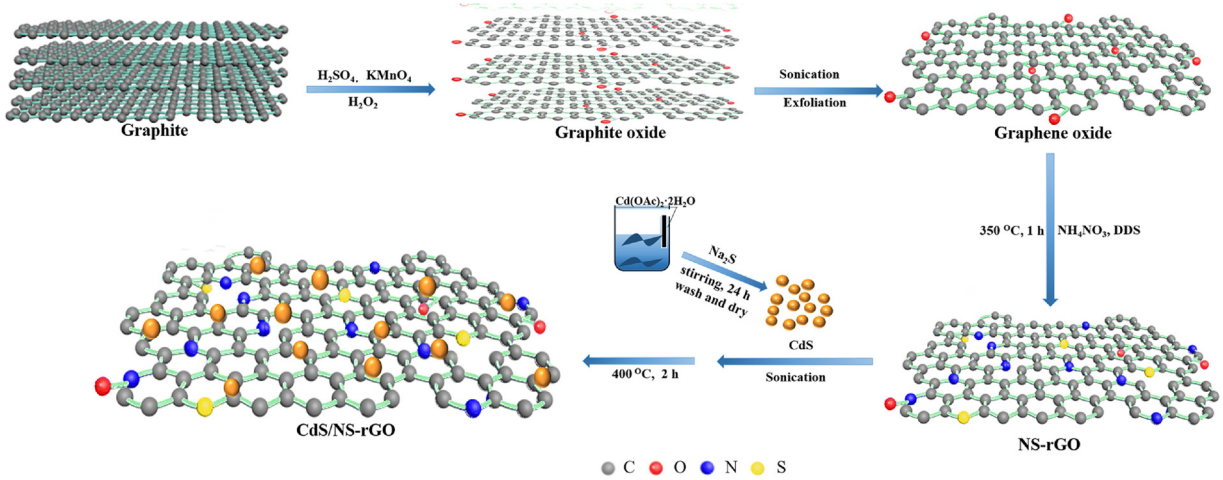

Fig. 1. Schematic illustration for the synthesis of CdS/NS-rGO nanocomposites.

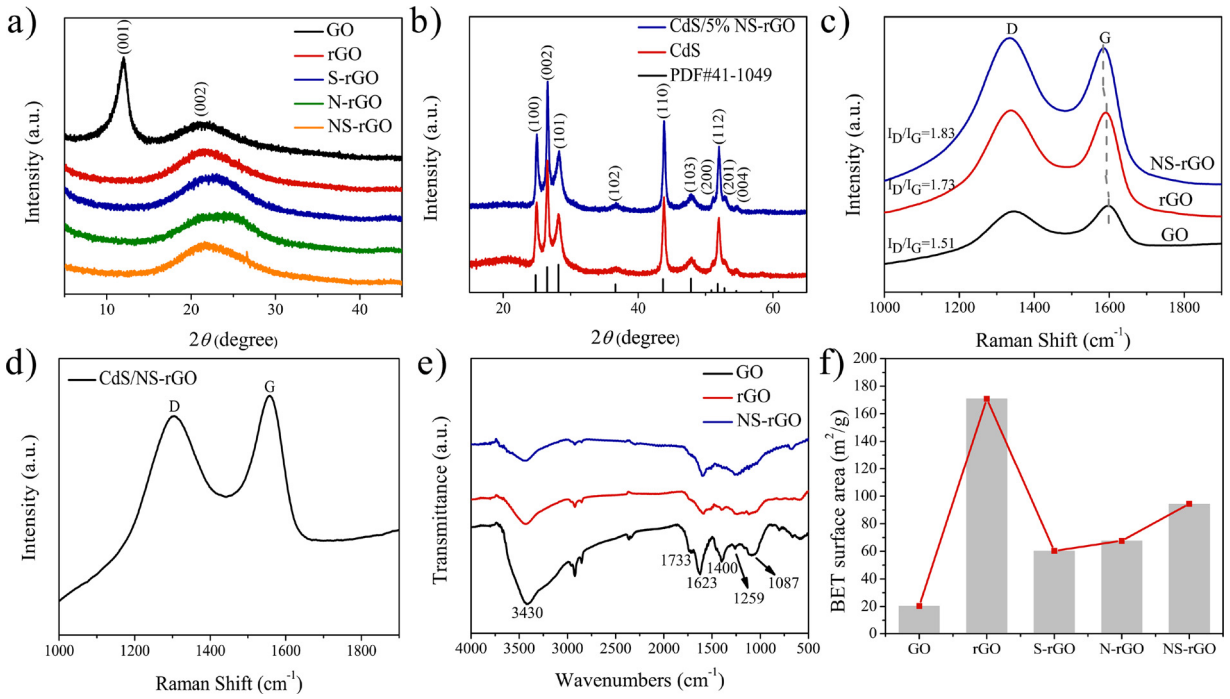

Fig. 2. XRD patterns of a) GO, rGO, S-rGO, N-rGO and NS-rGO and b) pure CdS and CdS/5%NS-rGO; c) Raman spectra of GO, rGO and NS-rGO; d) Raman spectra of CdS/NS-rGO; e) FT-IR spectra of GO, rGO and NS-rGO; f) BET specific surface area of various carbon materials.

simulation, the edge of graphene was filled with H atoms.

The adsorption energy of H atom ΔE_H was calculated by:

$$\Delta E_H = E_{surf+H} - E_{surf} - \frac{1}{2}E_{H_2}$$

in which ΔE_{surf+H} E_{surf+H} is the energy of surface adsorbed by H atom, ΔE_{surf} E_{surf} is the energy of the clean surface and E_{H_2} is the energy of a gas-phase hydrogen gas.

The Gibbs free energy of H adsorption was obtained by:

$$\Delta G_H = \Delta E_H + \Delta E_{ZPE} - T\Delta S_H$$

where ΔE_{ZPE} ΔE_{ZPE} is the zero-point energy and ΔS_H is the entropy. $\Delta E_{ZPE} - T\Delta S_H$ ΔE_{ZPE} - $T\Delta S_H$ eV in standard condition at T = 300 K [40].

Therefore, the ΔG_H ΔG_H was calculated by:

$$\Delta G_H = \Delta E_H + 0.28eV$$

2.4. Photocatalytic activity test

The photocatalytic H_2 production was conducted in a Pyrex reaction cell connected with an online photocatalytic hydrogen production system (CEL-SPH2N, CEAULight, Beijing). A 300 W Xe lamp (CEL-HXF300, CEAULight, Beijing) with a UV-cutoff filter ($\lambda \geq 420$ nm) was used as light source. 50 mg of the photocatalyst was dispersed in the lactic acid solution (10%). Prior to irradiation, the system was degassed 30 min in order to remove the dissolved air. The reaction temperature was controlled at 6–10 °C during the whole experiment. The generated H_2 was analyzed by an online gas chromatograph (GC-7920, CEAULight, China) equipped with a TCD detector.

Photocatalytic reduction of 4-NP was performed under the same light source. For a typical test, 20 mg photocatalyst and 50 mg ammonium formate (unless otherwise specified) were dispersed in 50 ml 4-NP solution (20 mg L^{-1}). Before exposure to light, the suspension was stirred in the dark for 2 h to allow the adsorption of reactant by the photocatalyst. During the reduction process, a N_2 flow (80 mL min^{-1}) was kept. 2 ml of sample solution was collected at a 2-min interval and immediately centrifuged to remove the catalyst at 12,000 rmp. Then, the centrifugal liquid was analyzed on a UV–vis spectrophotometer (UNICO UV-3802).

2.5. Photoelectrochemical measurements

The PEC measurements were performed in a standard three-electrode quartz cell using an electrochemical workstation (CHI660E, Chenhua, Shanghai). The fluorine-doped SnO_2 (FTO, < 15 Ω $square^{-1}$) glass electrode coated with samples was used as working electrode with an active area of 1.0 cm^2. The Pt plate and Ag/AgCl (saturated KCl) electrode were used as counter electrode and reference electrode, respectively. And 0.5 M Na_2SO_4 aqueous solution was used as the electrolyte. The working electrode was irradiated by a 300 W Xe lamp ($\lambda \geq 420$ nm, light intensity = 100 mW cm^{-2}) throughout the electrochemical test. Electrochemical impedance spectra (EIS) measurements were carried out in the presence of 0.1 M KCl solution containing 2.5 mM $K_3[Fe(CN)_6]/K_4[Fe(CN)_6]$ (1:1) mixture. The EIS Nyquist plots were collected over a frequency range of 0.1 Hz – 1000 kHz under open-circuit potential and modulation amplitude of 5 mV. The Mott-Schottky measurement was conducted from −0.8 to −0.5 V (vs. Ag/AgCl) with a frequency of 100 Hz in a 0.5 M Na_2SO_4 aqueous solution (pH = 6.8). The conversion from the measured potential vs. Ag/AgCl to the potential vs. normal hydrogen electrode (NHE) follows Nernst equation: E (NHE) = E (Ag/AgCl) + 0.197.

The preparation of working electrode was as follows: FTO conductive glass (1 cm × 2 cm) was cleaned in turn by ultrasonication in hexane, ethanol and deionized water for 15 min. 5 mg of the sample was ultrasonicated in 0.5 ml ethanol to form a homogenous suspension (10 mg mL^{-1}). The suspension was then coated onto FTO glass by drop-casting method with scotch tape as a spacer. After that, the scotch tape was removed, and the electrode was dried at 373 K for 0.5 h to improve the adhesion further.

3. Results and discussion

Fig. 2a displays the XRD patterns of these carbon materials. The XRD pattern of GO shows an sharp (001) diffraction peak at 10.9° due to the introduction of oxygen-containing functional groups. After the

thermal reduction and heteroatom doping, the characteristic peak at 10.9° disappears, and the left broad diffraction peaks of (002) was at ~22°, indicating a relatively larger interlayer spacing. This could be attributing to the lower doping temperature and the presence of some left functional groups between the layers (Fig. 2e) [41,42]. XRD patterns of pure CdS, CdS/5%NS-rGO nanocomposite, and the standard diffraction pattern of hexagonal CdS are shown in Fig. 2b. The diffraction peaks for CdS correspond to the hexagonal CdS (JCPDS Card No. 41–1049). No obvious difference could be found between CdS and CdS/5%NS-rGO due to the weak response and low percentage of NS-rGO [4,43,44].

Raman spectra is effective tool to study the structural defect for carbon-based materials. The two characteristic peaks at about 1340 and 1590 cm^{-1} can be observed in all samples, corresponding to the D band and G band of rGO (Fig. 2c). It is well known that the D band arises from the defects and disorder of C atoms, while the G band is related to sp^2 carbon bond structure. The intensity ratio of D to G (I_D/I_G) is used to represent the defect level of carbon crystals [29,45]. According to Fig. 2c, rGO has a higher I_D/I_G value (1.73) than that of GO (1.51). And the I_D/I_G value of NS-rGO can be increased to 1.83 after the heteroatom co-doping of N and S. Moreover, the G band shows a blue shift from 1596.5 to 1584.6 cm^{-1}. The increasing of I_D/I_G as well as the blue shift of G band indicates that a large number of defect sites has been introduced during the doping process [46,47]. The Raman spectrum in Fig. 2d shows the typical D peak and G peak for graphitized structure, approving the presence of NS-rGO in the CdS/NS-rGO. The FT-IR spectra of GO, rGO and NS-rGO is shown in Fig. 2e, the characteristic peaks at 3430, 1733, 1623, 1400, 1259 and 1087 cm^{-1} for GO are assigned to O—H stretching vibration, C═O stretching vibration, C═C stretching vibration, O—H bending vibration, C—O stretching vibrations, respectively [48]. After reduction process, the intensities of these peaks decreased obviously, indicating the successful removal of the oxygen containing groups.

Fig. 2f and S1 show N_2 adsorption results for these samples. Generally, the thermal annealing can cause violent expansion and further exfoliation of graphene layers, leading to the suface area (SSA) increasing. While the exfoliation degree will be inhibited when nitrogen and sulfur precursors were added during the heating process, resulting in the decreased SSA [29]. The N_2 adsorption isotherms and the corresponding pore size distribution curves (inset) of CdS and CdS/5%NS-rGO samples are given in Fig. S1b. Their isotherms type are identified as type IV, proving their mesoporous structure [49]. Little improvement in adsorption capability was made for the CdS/5%NS-rGO composite, probably due to the low percentage of NS-rGO dosed. The pore size is similar, which should be resulted from the gaps between the aggregated CdS nanoparticles [50].

Fig. 3 shows the TEM images of samples. As shown in Fig. 3a, TEM image of CdS nanoparticles displays a significant aggregation with particle size of 20–30 nm. Fig. 3b shows the TEM image of NS-rGO with wrinkle and transparent layers. Fig. 3c–d show the TEM images of CdS/NS-rGO composite with different magnifications. The CdS nanoparticles are observed to be uniformly distributed on the surface of NS-rGO sheets. The HRTEM images of CdS/NS-rGO are shown in Fig. 3e, and a close contact between CdS and NS-rGO sheets could be found. The interlayer spacing of 0.335 nm corresponds to the (002) plane of hexagonal CdS (inset of Fig. 3e). In addition, the corresponding selected area electron diffraction (SAED) pattern of CdS/NS-rGO (Fig. 3f) shows diffraction rings, indicating that CdS/NS-rGO nanocomposite possess polycrystalline structure. The diffraction rings can be indexed to the (002) and (110) planes of CdS, corresponding to the XRD results in Fig. 2b.

XPS was then employed to investigate the surface chemical compositions and bonding state of NS-rGO. Fig. 4a shows the survey XPS spectra of NS-rGO. Obvious N and S peaks can be clearly detected with the atomic percentage of 7.22 and 1.34 at% in NS-rGO sample, indicating the successful doping into the rGO sheets. As shown in Fig. 4b, the strong peak at 284.8 eV corresponds to sp^2 carbon, and the peak at 286.1 eV is due to the sp^2 carbon bonded with heteroatoms. The peaks at 287.0 and 288.3 eV are assigned to C═O/C—O—C and O—C═O, respectively [26,51,52]. The high resolution XPS of N1s in Fig. 4c exhibits three peaks, attributing to pyridinic N (398.6 eV), pyrrolic N (400.0 eV), and graphitic N (401.6 eV), respectively [53,54]. Fig. 4d shows the S2p spectrum, which can be deconvoluted into four peaks located at 163.8, 164.9, 167.9 and 170.0 eV. The first two peaks are origin from the $2p_{3/2}$ and $2p_{1/2}$ of thiophene S (resulting from the spin-orbit splitting), corresponding to C—S_x—C and C═S bonds. The other two peaks with higher bind energy should arise from oxidized S [55–58]. We also investigated the relative content of S and N elements in NS-rGO samples with different doping ratio of nitrogen and sulfur dopants. As shown in Table S1, the doping content of S increases from 0.21 to 2.09 at% with the addition of DDS from 0.05 to 0.5 g. The XPS survey spectrum of the CdS/NS-rGO sample in Fig. S2 shows the existence of Cd, S, C, O, N and S elements in CdS/NS-rGO. The N1s peak (inset in Fig. S2) is overlapped by the strong Cd3d peak [59].

The photocatalytic performance of CdS/NS-rGO composites was then investigated for the H_2 evolution and 4-NP reduction into 4-aminophenol (4-AP). The photocatalytic H_2 evolution was carried out under visible light irradiation ($\lambda \geq 420$ nm) using lactic acid as the sacrificial agent. The H_2 evolution rates of CdS and CdS/NS-rGO with different NS-rGO percentage are shown in Fig. 5a. CdS is a visible light response n-type semiconductor, but CdS alone has weak photo-activity for H_2 evolution. The pure CdS has a relative low H_2 evolution rate of 292 μmol h^{-1} g^{-1} due to the fast recombination of photogenerated electron-hole pairs. Loading NS-rGO as cocatalyst on CdS could obtain increased photocatalytic activity. Increasing the percentage of NS-rGO, the photocatalytic H_2 evolution rate could increase gradually. The highest value could reach as more as 1701 μmol h^{-1} g^{-1} for CdS/5%NS-rGO, which is about 5.8 times higher than that for pure CdS. However, a declining H_2 evolution activity is observed with the further increased NS-rGO percentage. In particular, with the NS-rGO content at 10%, the photocatalytic activity is even worse than pure CdS. Increasing the percent of dark NS-rGO cocatalyst will shield the active sites of CdS as well as decrease the depth of light penetration into the photocatalyst and the solution. Such a “shielding effect” would weaken the photocatalytic activity of the CdS/NS-rGO [22,25,28]. The heteroatom doping will break the chemical inertness of rGO and increase its cocatalytic activity [60]. On the other hand, the doping process will also introduce asymmetric structure, leading to the stability decreasing. As shown in Fig. 5b, the stability test of the optimized CdS/5%NS-rGO photocatalyst was conducted for a long time duration (20 h). In the fourth 5 h, the generated h_2 was decreased to ~76.6% compared to the first 5 h, which is lower than the CdS/5%rGO (83.2%, Fig. S3).

To confirm the superiority of NS-rGO, CdS/GO, CdS/rGO, CdS/S-rGO and CdS/N-rGO samples were also tested for comparison. All samples were loading with 5 wt% content of corresponding carbon materials. As shown in Fig. 5c, CdS/NS-rGO exhibits much higher H_2 evolution activity than other samples. The photocatalytic activity order is as follows: CdS/NS-rGO > CdS/N-rGO > CdS/S-rGO > CdS/rGO > CdS/GO. The results indicate that the cocatalytic activities can be increased with the doping of nitrogen atoms compared to the thermal reduced rGO. This enhancement effect could be further increased by combination with sulfur and nitrogen doping at the same time. In addition, the cocatalytic effect could also be varied by adjusting the ratios of doped sulfur and nitrogen. The effect of doping ratio between nitrogen and sulfur dopants on photocatalytic activity is shown in Fig. 5d. The photocatalytic activity increased with the addition of DDS from 0.05 to 0.3 g, and then decreased with the further increasing of DDS addition amount. It was proposed that co-doped graphene with proper proportion of nitrogen and sulfur atoms can change the electron distribution and increase the charge density of some point on the surface. These points could be used as active sites for H_2 generation. This density will however decrease with more sulfur atoms doping [29].

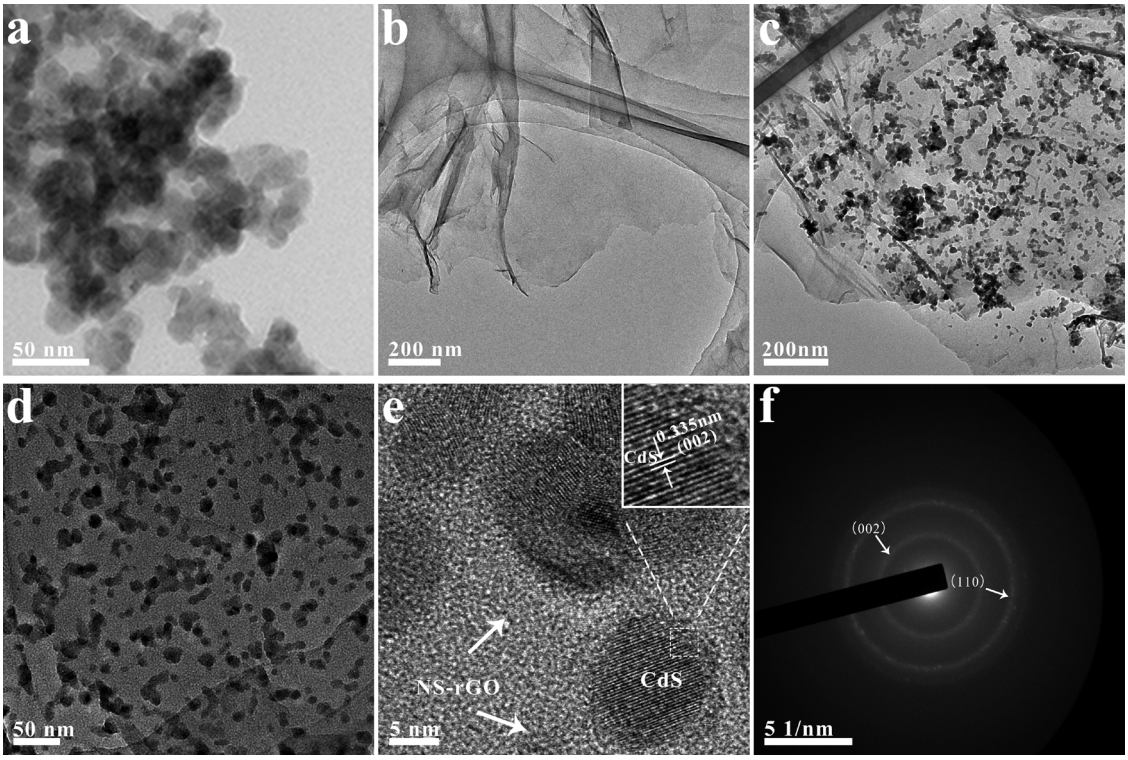

Fig. 3. a) TEM image of CdS nanoparticles; b) TEM image of NS-rGO sheets; c) and d) TEM images of CdS/NS-rGO nanocomposite; e) HRTEM image of CdS/NS-rGO nanocomposite (inset of e is the HRTEM image for the selected single CdS particle); f) SAED pattern of CdS/NS-rGO nanocomposite.

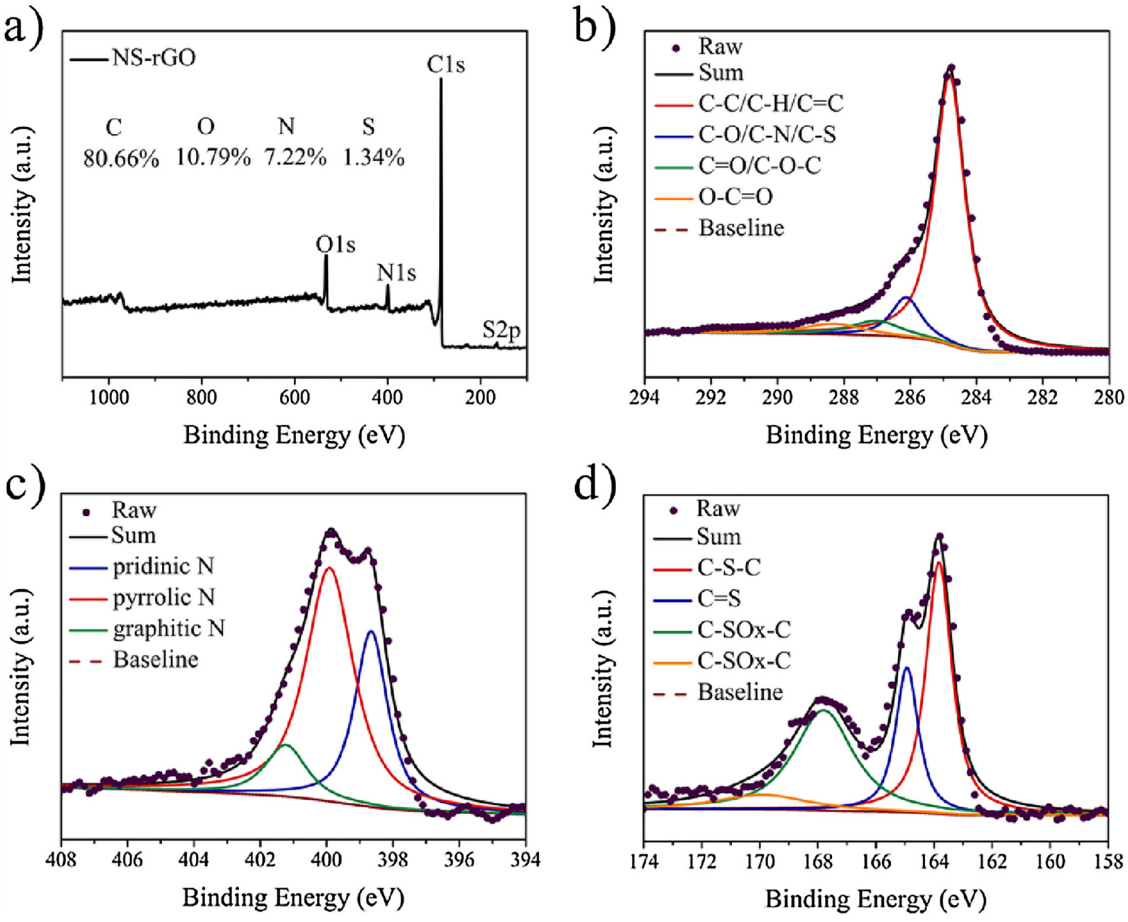

Fig. 4. a) XPS survey spectra of the NS-rGO sample; the corresponding high resolution XPS spectra of b) C1s, c) N1s and d) S2p.

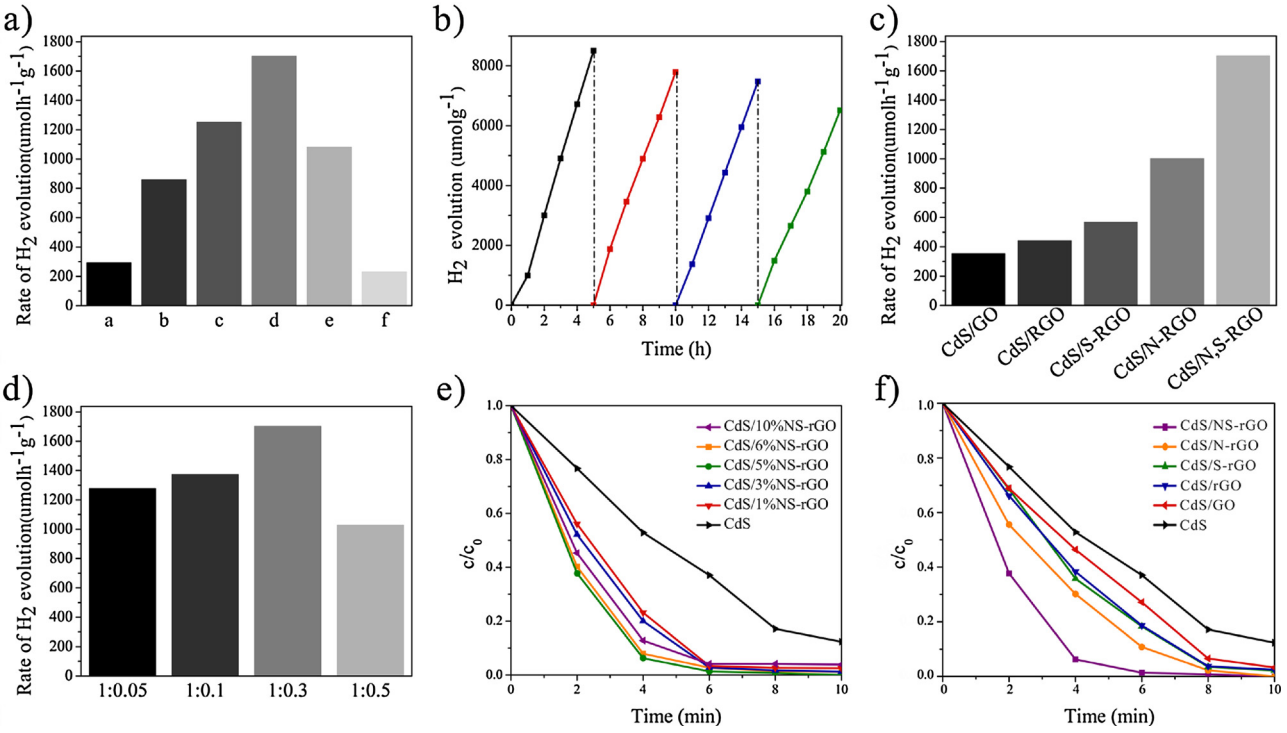

Fig. 5. a) Hydrogen evolution rate of different photocatalysts: a) pure CdS, b) CdS/1%NS-rGO, c) CdS/3%NS-rGO, d) CdS/5%NS-rGO, e) CdS/6%NS-rGO, f) CdS/10%NS-rGO; b) Cyclic test of H_2 evolution for CdS/5%NS-rGO photocatalyst; c) Hydrogen evolution rate of different carbon materials-based CdS photocatalysts; d) The hydrogen evolution rate of CdS/5%NS-rGO photocatalysts with different weight ratios of nitrogen precursor to sulfur precursor; Photocatalytic reduction of 4-NP over e) CdS/NS-rGO photocatalysts with different NS-rGO percentages and f) different carbon materials-based CdS photocatalysts.

The photocatalytic performance of CdS/NS-rGO was also evaluated by reduction of 4-NP to corresponding 4-AP in water with the addition of ammonium formate as the sacrificial agent. Fig. 5e shows the test results (c/c_0) over CdS/NS-rGO nanocomposites with different percentages of NS-rGO. Similar to photocatalytic hydrogen production discussed above, a proper percentage of NS-rGO can effectively improve photocatalytic activity for this reduction, while adding more cocatalyst will however decrease the activity. The optimum percentage of NS-rGO is 5%, the same as that for photocatalytic H_2 evolution. Almost all of 4-NP was reduced over CdS/5%NS-rGO within 6 min under visible light irradiation, whereas pure CdS only reduced about 62% of 4-NP in the same time. The comparison of CdS/NS-rGO with other carbon materials-based CdS photocatalysts is displayed in Fig. 5f. A similar activity order could be found with H_2 generation. The reduction efficiency of 4-NP was also effected by the dosage of the sacrificial reagent (Fig. S4). The presence of ammonium formate could prevent the photocorrosion of CdS by capturing photogenerated holes. More sacrificial agent can therefore increase the photocatalytic reduction rate.

To further confirm the photocatalytic enhancement mechanism, transient photocurrent response of the samples was tested. As shown in Fig. 6a, photocurrents could be observed for all these samples under visible light irradiation, and the photocurrent rapidly drops to zero once the light is cut off. Notably, the order of the photocurrents is consistent with aforementioned photocatalytic performance. CdS/NS-rGO exhibits much higher photocurrent density than other samples, indicating that the NS-rGO is the best cocatalyst for charge separation and transfer.

Electrochemical impedance spectra (EIS) can be used to analyze the charge transfer process on the semiconductor/electrolyte interface. Fig. S5 shows the EIS spectra of rGO and NS-rGO, and the charge transfer resistance of NS-rGO at the electrode/electrolyte interface is smaller (~37 Ω) compared to the rGO of ~95 Ω, indicating the improved electrical conductivity of NS-rGO. The EIS Nyquist plots of CdS and CdS/5%NS-rGO samples are shown in Fig. 6b. Both of these two samples include two semi-cycles and a diagonal. In the equivalent circuit (inset), R1 represents the electrolyte resistance. The first semicircle can be ascribe to the interface impedance R2 and interface capacitance CPE1 of the solid-state interface layer formed in the passivation reaction. The charge transfer resistance R3 (equivalent to the second semicycle diameter) and the capacitance of the electrode/electrolyte double layer CPE2 correspond to the second semicircle, while W1 is the Warburg impedance origin from the diffusion of ions [61–63]. Obviously, CdS/5%NS-rGO has smaller arc radius than that of CdS (especially the second semicircle), indicating smaller charge transfer resistance [50,64]. Therefore, photogenerated electrons from CdS can transfer quickly onto the NS-rGO sheets under visible light excitation, thus suppressing the recombination of photogenerated electron-hole pairs and enhancing the photoelectric conversion efficiencies of composites. PL emission spectra of the photocatalysts are shown in Fig. 6c, which can reveal the efficiency of electron-hole separation [65,66]. It can be seen that CdS displays a strong PL emission peak at about 560 nm. The strong peak is origin from the fast recombination of photogenerated electron-hole pairs, leading to the weak photo-activity. After combination with rGO or NS-rGO as cocatalysts, the characteristic PL peaks decreased obviously, attributing to the excellent charge transfer ability of NS-rGO. Fig. 6d presents the corresponding time-resolved PL decay spectrum. The shorter fluorescence lifetime of CdS/NS-rGO proves the less recombination probability of the composites further.

The UV–vis diffuse reflectance spectra (DRS) for the samples is displayed in Fig. 7a. Enhanced absorption ability in the visible light region can be observed for CdS/rGO and CdS/NS-rGO. In addition, the absorption edge red-shift obviously after loading with NS-rGO. These changes will increase the utilization efficiency toward the light source. The absorption of NS-rGO is very weak, and no absorption peaks could be found. The addition of NS-rGO would only impose a wide background absorption in the visible light region slightly. The change of absorption range should be therefore origin from the intimate

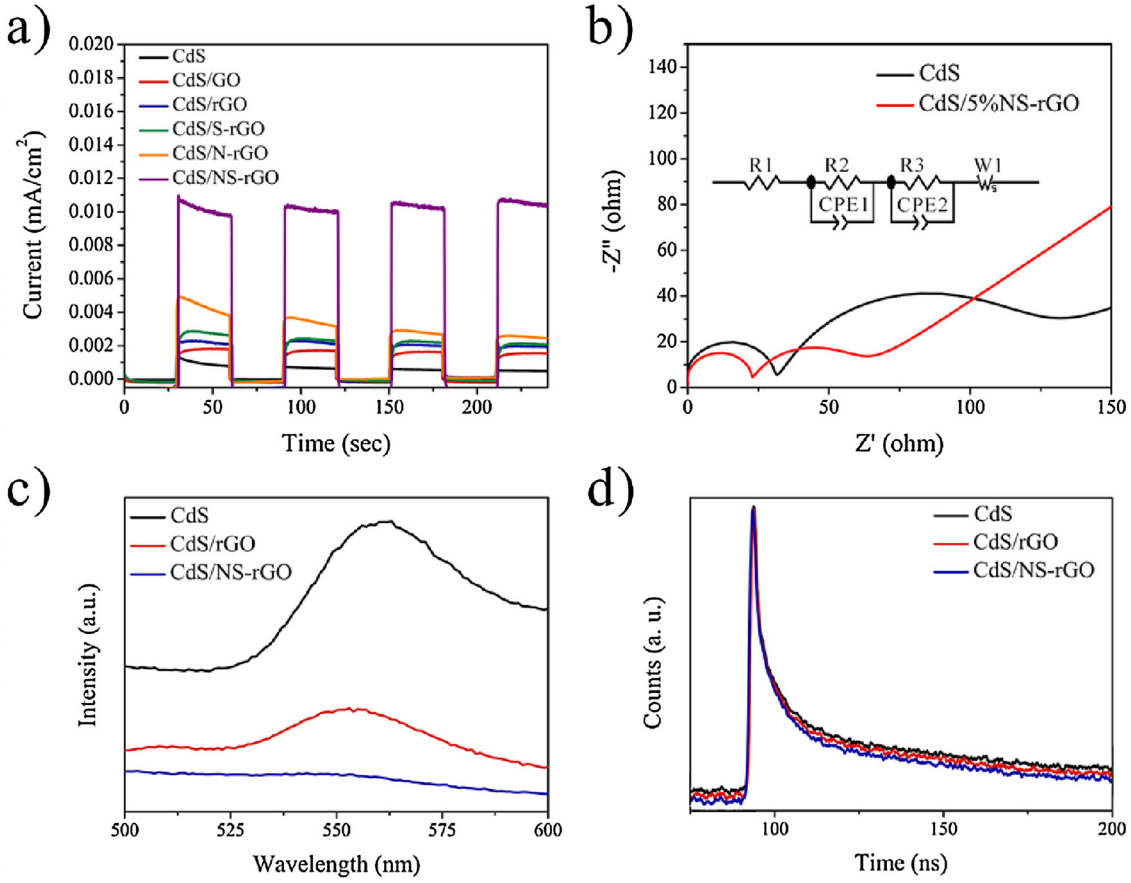

Fig. 6. a) Transient photocurrent responses of CdS and carbon materials-based CdS photocatalysts under visible light irradiation at 0 V vs. Ag/AgCl; b) Electrochemical impedance spectra (EIS) of CdS and CdS/5%NS-rGO modified electrodes (The inset shows the equivalent circuit); c) Photoluminescence (PL) spectra and d) Time-resolved fluorescence decay curves of CdS, CdS/rGO and CdS/NS-rGO.

electronic interaction and charge equilibration between CdS and NS-rGO [67,68]. According to the corresponding plots of transformed Kubelka-Munk function vs. photon energy (Fig. 7b) [69], the band gap for pristine CdS is about 2.02 eV, while that for CdS/rGO and CdS/NS-rGO nanocomposite decreased to 1.90 and 1.82 eV, respectively. Compared to the rGO, the NS-rGO has improved conductivity due to the extra p-electrons that nitrogen and sulfur atoms contribute to the systems. Therefore, NS-rGO can be used as more ideal electron sink or electron transfer media [60]. Photo-induced electron-hole pairs could then migrate rapidly to the surface of NS-rGO to retard electron-hole recombination, thereby enhancing photo-activity. On the other hand, the presence of N and S atoms could provide more anchor sites and establish more intimate interfacial contact between CdS and NS-rGO. The electronic interaction and charge equilibration between CdS and NS-rGO could led to more obvious shift in the Fermi level and more narrowed band gap [70,71].

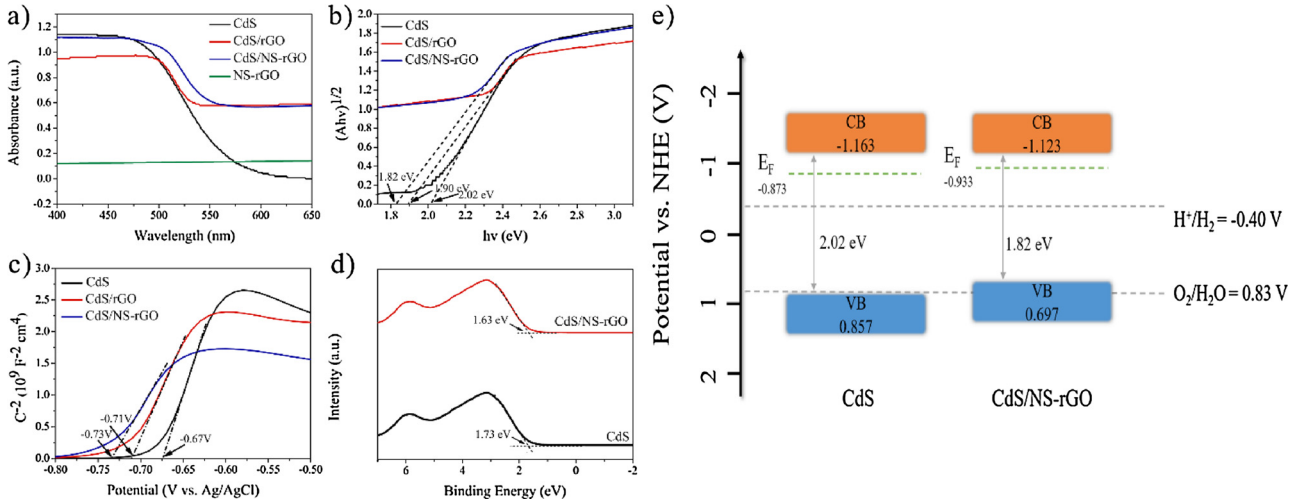

Fig. 7. a) UV–vis diffusive reflectance spectra (DRS); b) Corresponding plots of transformed Kubelka-Munk function vs. photon energy and c) Mott-Schottky plots of CdS, CdS/rGO and CdS/NS-rGO; d) Valence band XPS spectra and e) Proposed band structures of CdS and CdS/NS-rGO.

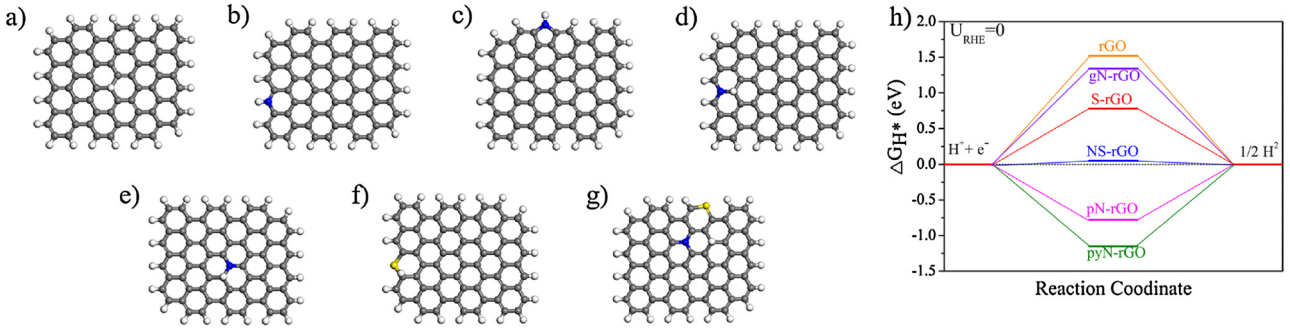

Fig. 8. The structure model of (a) rGO; (b–e) doped rGO with nitrogen (blue) (b) pyridinic N, c) pyrrolic N, d and e) graphitic N); (f) doped rGO with sulfur (yellow); (g) doped rGO with nitrogen and sulfur; (h) calculated HER free energy diagram at equilibrium potential for rGO, pyridinic N (pN-rGO), pyrrolic doped N (pyN-rGO), graphitic doped N (gN-rGO), S-rGO, and NS-rGO. (For interpretation of the references to color in this figure legend, the reader is referred to the web version of this article).

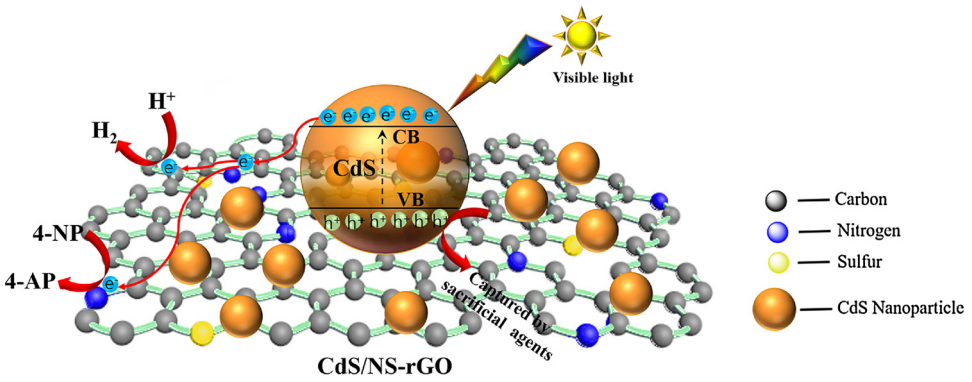

Fig. 9. Schematic illustration of proposed mechanism for the photocatalytic reaction process over CdS/NS-rGO photocatalyst under visible light.

Additionally, the Mott-Schottky plots for the CdS, CdS/rGO and CdS/NS-rGO electrodes were investigated to characterize electron donor density (N_d) and flat band potential (E_{fb}). As shown in Fig. 7**c**, positive slopes suggest that the incorporation of rGO and NS-rGO won't affect the n-type semiconductor nature of CdS, which agrees with previous reports [61,72,73]. The E_{fb} are −0.67, −0.71 and −0.73 V vs. Ag/AgCl (−0.47, −0.51 and −0.53 V vs. NHE) for CdS, CdS/rGO and CdS/NS-rGO, respectively. Moreover, the N_d (inversely proportional to the slope) of CdS/NS-rGO is higher than that of CdS, indicating a more effective separation of electrons and holes. Fig. 7d shows the valence band XPS (VB XPS) spectra of CdS and CdS/NS-rGO. It could be calculated that the energy distances between the Fermi level (E_F) and valence band maximum are 1.73 and 1.63 eV for these two samples [74,75]. Based on the results of band gaps, Mott-Schottky plots and VB XPS, the approximate energy band structures of CdS and CdS/NS-rGO are described in Fig. 7e. The conduction band energies (E_{CB}) were determined following from the equation $E_g = E_{VB} - E_{CB}$. Obviously, with the addition of NS-rGO, smaller band gaps could be obtained, thus leading to the enhanced photo-activity.

To understand the enhancement mechanism of NS-rGO as cocatalyst, density functional theory (DFT) calculations were used to calculate the H* absorption free energy (ΔG_{H^*}) of both pristine graphene and N, S co-doped graphene. The structure model of the samples are shown in Fig. 8a–g, which refers to previous literatures [29,76]. And the corresponding ΔG_{H^*} are shown in Fig. 8h. For hydrogen generation reaction, the catalyst whose $|\Delta G_H{}^*|$ is close to 0 should be optimal. $|\Delta G_{H^*}|$ of undoped rGO is largest (1.52 eV), indicating a weak electrochemical HER activity. Doped with N or S will decrease the $|\Delta G_{H^*}|$, thus increasing the electrochemical HER activity. Indeed, it is impossible to obtain single chemical environment N-doped graphene in experiment. However, in DFT calculation, we could analyze the influence of different chemical environment N on H* adsorption free energies by building pyridinic N, pyrrolic N, and graphitic N, respectively. They are −0.78 eV, −1.15 eV, and 1.34 eV, separately. The real $|\Delta G_{H^*}|$ of doped N should between 0.78 eV and 1.34 eV, while the $|\Delta G_{H^*}|$ of NS-rGO is 0.05 eV, closest to 0. The photocatalytic H_2 evolution is also an electrochemical HER process with the photo-generated electrons as the electric source. The small $|\Delta G_{H^*}|$ of NS-rGO is therefore an important cause for its good cocatalytic activity.

It was reported that adding foreign heteroatoms with a different electronegativity than carbon will break the electroneutrality in graphene and create unbalanced charged areas which could serve as active sites [77]. The on-site bader charges of carbon atoms were also calculated for NS-rGO (Fig. S6 and Table S2). It was found that some of the carbon atoms near the dopants are negatively charged. These negatively charged carbon atoms is favorable to capture of the H^+ and electron withdrawing –NO_2 group. These carbon atoms as well as some structure defects could be the active sites for H_2 generation and 4-nitrophenol reduction [78]. Based on the aforementioned results, the photocatalysis mechanism on the optimized CdS/NS-rGO composite is proposed in Fig. 9. The electron-hole pairs are separated in CdS under visible light illumination. The generated electrons will transfer onto the surface of NS-rGO rapidly due to its good conductivity. The presence of heteroatoms will produce amounts of active sites, which will accept the transferred electrons for H_2 generation or 4-NP reduction. While the remaining holes are captured by the sacrificial agent at the same time.

4. Conclusions

In summary, the NS-rGO was synthesized using a facile calcination method at a low temperature, which is effective to promote the photocatalytic activity of CdS. The presence of NS-rGO could increase the SSA and provide more active sites for H_2 generation and 4-nitropheonl reduction. In addition, loading CdS on NS-rGO, better charge separation

efficiency, wider light absorption range, smaller band gap, and decreased H* absorption free energy could be achieved, thus leading to an enhanced photo-activity. The novel CdS/NS-rGO composite without noble metals is proven to be a low-cost and promising catalyst material for the photocatalytic H_2 generation and 4-NP reduction under visible light.

Acknowledgment

This research was supported by the project No. 21506158 from the National Natural Science Foundation of China (NSFC).

Appendix A. Supplementary data

Supplementary material related to this article can be found, in the online version, at doi:https://doi.org/10.1016/j.apcatb.2018.05.021.

References

[1] X. Zhang, L. Li, S. Wen, H. Luo, C. Yang, Design and synthesis of multistructured three-dimensionally ordered macroporous composite bismuth oxide/zirconia: photocatalytic degradation and hydrogen production, J. Colloid Interface Sci. 499 (2017) 159–169.
[2] M. Matsuoka, M. Kitano, M. Takeuchi, K. Tsujimaru, M. Anpo, J.M. Thomas, Photocatalysis for new energy production, Catal. Today 122 (2007) 51–61.
[3] S. Cao, J. Yu, g-C_3N_4-based photocatalysts for hydrogen generation, J. Phys. Chem. Lett. 5 (2014) 2101–2107.
[4] W.C. Peng, Y. Chen, X.Y. Li, MoS_2/reduced graphene oxide hybrid with CdS nanoparticles as a visible light-driven photocatalyst for the reduction of 4-nitrophenol, J. Hazard. Mater. 309 (2016) 173–179.
[5] H. Yu, Y. Zhao, C. Zhou, L. Shang, Y. Peng, Y. Cao, L.Z. Wu, C.H. Tung, T. Zhang, Carbon quantum dots/TiO2 composites for efficient photocatalytic hydrogen evolution, J. Mater. Chem. A 2 (2014) 3344.
[6] L.L. Tan, S.P. Chai, A.R. Mohamed, Synthesis and applications of graphene-based TiO_2 photocatalysts, ChemSusChem 5 (2012) 1868–1882.
[7] F. Guo, W. Shi, W. Guan, H. Huang, Y. Liu, Carbon dots/g-C_3N_4/ZnO nanocomposite as efficient visible-light driven photocatalyst for tetracycline total degradation, Sep. Purif. Technol. 173 (2017) 295–303.
[8] J. Wang, Y. Xia, H. Zhao, G. Wang, L. Xiang, J. Xu, S. Komarneni, Oxygen defects-mediated Z-scheme charge separation in g-C_3N_4/ZnO photocatalysts for enhanced visible-light degradation of 4-chlorophenol and hydrogen evolution, Appl. Catal. B-Environ. 206 (2017) 406–416.
[9] A. Ye, W. Fan, Q. Zhang, W. Deng, Y. Wang, CdS–graphene and CdS–CNT nanocomposites as visible-light photocatalysts for hydrogen evolution and organic dye degradation, Catal. Sci. Technol. 2 (2012) 969.
[10] H. Li, X. Wang, J. Xu, Q. Zhang, Y. Bando, D. Golberg, Y. Ma, T. Zhai, One-dimensional CdS nanostructures: a promising candidate for optoelectronics, Adv. Mater. 25 (2013) 3017–3037.
[11] R. Bera, S. Kundu, A. Patra, 2D hybrid nanostructure of reduced graphene oxide-CdS nanosheet for enhanced photocatalysis, ACS App. Mater. Interfaces 7 (2015) 13251–13259.
[12] F. Ma, Y. Wu, Y. Shao, Y. Zhong, J. Lv, X. Hao, 0D/2D nanocomposite visible light photocatalyst for highly stable and efficient hydrogen generation via recrystallization of CdS on MoS_2 nanosheets, Nano Energy 27 (2016) 466–474.
[13] J. Ran, J. Zhang, J. Yu, M. Jaroniec, S.Z. Qiao, Earth-abundant cocatalysts for semiconductor-based photocatalytic water splitting, Chem. Soc. Rev. 43 (2014) 7787–7812.
[14] T. Simon, N. Bouchonville, M.J. Berr, A. Vaneski, A. Adrovic, D. Volbers, R. Wyrwich, M. Doeblinger, A.S. Susha, A.L. Rogach, F. Jackel, J.K. Stolarczyk, J. Feldmann, Redox shuttle mechanism enhances photocatalytic H_2 generation on Ni-decorated CdS nanorods, Nat. Mater. 13 (2014) 1013–1018.
[15] N. Bao, L. Shen, T. Takata, K. Domen, A. Gupta, K. Yanagisawa, C.A. Grimes, Facile Cd-thiourea complex thermolysis synthesis of phase-controlled CdS nanocrystals for photocatalytic hydrogen production under visible light, J. Phys. Chem. C 111 (2007) 17527–17534.
[16] D. Lang, Q. Xiang, G. Qiu, X. Feng, F. Liu, Effects of crystalline phase and morphology on the visible light photocatalytic H(2)-production activity of CdS nanocrystals, Dalton Trans. 43 (2014) 7245–7253.
[17] X. Fan, G. Zhang, F. Zhang, Multiple roles of graphene in heterogeneous catalysis, Chem. Soc. Rev. 44 (2015) 3023–3035.
[18] X.Q. An, J.C. Yu, Graphene-based photocatalytic composites, RSC Adv. 1 (2011) 1426–1434.
[19] N. Zhang, Y.H. Zhang, Y.J. Xu, Recent progress on graphene-based photocatalysts: current status and future perspectives, Nanoscale 4 (2012) 5792–5813.
[20] Q.J. Xiang, J.G. Yu, M. Jaroniec, Graphene-based semiconductor photocatalysts, Chem. Soc. Rev. 41 (2012) 782–796.
[21] X. Li, J. Yu, S. Wageh, A.A. Al-Ghamdi, J. Xie, Graphene in photocatalysis: a review, Small 12 (2016) 6640–6696.
[22] Q. Li, B. Guo, J. Yu, J. Ran, B. Zhang, H. Yan, J.R. Gong, Highly efficient visible-light-driven photocatalytic hydrogen production of CdS-cluster-decorated graphene nanosheets, J. Am. Chem. Soc. 133 (2011) 10878–10884.
[23] L.K. Putri, W.-J. Ong, W.S. Chang, S.-P. Chai, Heteroatom doped graphene in photocatalysis: a review, Appl. Surf. Sci. 358 (2015) 2–14.
[24] W. Han, Z. Li, Y. Li, X. Fan, F. Zhang, G. Zhang, W. Peng, The promoting role of different carbon allotropes cocatalysts for semiconductors in photocatalytic energy generation and pollutants degradation, Front. Chem. 5 (2017) 84.
[25] C.H. Choi, M.W. Chung, H.C. Kwon, S.H. Park, S.I. Woo, B, N- and P, N-doped graphene as highly active catalysts for oxygen reduction reactions in acidic media, J. Mater. Chem. A 1 (2013) 3694–3699.
[26] B. Han, S. Liu, Z.-R. Tang, Y.-J. Xu, Electrostatic self-assembly of CdS nanowires-nitrogen doped graphene nanocomposites for enhanced visible light photocatalysis, J. Energy Chem. 24 (2015) 145–156.
[27] C. Han, X. Bo, Y. Zhang, M. Li, L. Guo, One-pot synthesis of nitrogen and sulfur co-doped onion-like mesoporous carbon vesicle as an efficient metal-free catalyst for oxygen reduction reaction in alkaline solution, J. Power Sources 272 (2014) 267–276.
[28] Z. Yang, K. Qian, J. Lv, W. Yan, J. Liu, J. Ai, Y. Zhang, T. Guo, X. Zhou, S. Xu, Z. Guo, Encapsulation of Fe_3O_4 nanoparticles into N, S co-doped graphene sheets with greatly enhanced electrochemical performance, Sci. Rep. 6 (2016) 27957.
[29] X. Duan, K. O'Donnell, H. Sun, Y. Wang, S. Wang, Sulfur and nitrogen co-doped graphene for metal-free catalytic oxidation reactions, Small 11 (2015) 3036–3044.
[30] K.G. Qu, Y. Zheng, X.X. Zhang, K. Davey, S. Dai, S.Z. Qiao, Promotion of electrocatalytic hydrogen evolution reaction on nitrogen-doped carbon nanosheets with secondary heteroatoms, ACS Nano 11 (2017) 7293–7300.
[31] Q. Li, X. Li, S. Wageh, A.A. Al-Ghamdi, J. Yu, CdS/graphene nanocomposite photocatalysts, Adv. Energy Mater. (2015) 5.
[32] W.S. Hummers Jr, R.E. Offeman, Preparation of graphitic oxide, J. Am. Chem. Soc. 80 (1958) 1339.
[33] J.P. Perdew, K. Burke, M. Ernzerhof, Generalized gradient approximation made simple, Phys. Rev. Lett. 77 (1996) 3865.
[34] G. Kresse, J. Furthmüller, Efficiency of ab-initio total energy calculations for metals and semiconductors using a plane-wave basis set, Comput. Mater. Sci. 6 (1996) 15–50.
[35] G. Kresse, J. Furthmüller, Efficient iterative schemes for ab initio total-energy calculations using a plane-wave basis set, Phys. Rev. B. 54 (1996) 11169.
[36] G. Kresse, G. Hafner, Ab initio molecular dynamics for liquid metals, Phys. Rev. B. 47 (1993) 558.
[37] P.E. Blöchl, Projector augmented-wave method, Phys. Rev. B. 50 (1994) 17953.
[38] G. Kresse, D. Joubert, From ultrasoft pseudopotentials to the projector augmented-wave method, Phys. Rev. B. 59 (1999) 1758–1775.
[39] O. Bengone, M. Alouani, P. Blöchl, J. Hugel, Implementation of the projector augmented-wave LDA+U method: application to the electronic structure of NiO, Phys. Rev. B. 62 (2000) 16392–16401.
[40] J.K. Nørskov, T. Bligaard, A. Logadottir, J.R. Kitchin, J.G. Chen, S. Pandelov, U. Stimming, Trends in the exchange current for hydrogen evolution, J. Electrochem. Soc. 152 (2005) J23–J26.
[41] Z.H. Sheng, S. Lin, J.J. Chen, W.J. Bao, F.B. Wang, X.H. Xia, Catalyst-free synthesis of nitrogen-doped graphene via thermal annealing graphite oxide with melamine and its excellent electrocatalysis, ACS Nano 5 (2011) 4350–4358.
[42] W.N. Yan, X.C. Cao, J.H. Tian, C. Jin, K. Ke, R.Z. Yang, Nitrogen/sulfur dual-doped 3D reduced graphene oxide networks-supported CoFe2O4 with enhanced electrocatalytic activities for oxygen reduction and evolution reactions, Carbon 99 (2016) 195–202.
[43] N. Zhang, M.Q. Yang, Z.R. Tang, Y.J. Xu, CdS–graphene nanocomposites as visible light photocatalyst for redox reactions in water: a green route for selective transformation and environmental remediation, J. Catal. 303 (2013) 60–69.
[44] X. Bai, C. Sun, D. Liu, X. Luo, D. Li, J. Wang, N. Wang, X. Chang, R. Zong, Y. Zhu, Photocatalytic degradation of deoxynivalenol using graphene/ZnO hybrids in aqueous suspension, Appl. Catal. B- Environ. 204 (2017) 11–20.
[45] Z. Li, Y. Pi, D. Xu, Y. Li, W. Peng, G. Zhang, F. Zhang, X. Fan, Utilization of MoS_2 and graphene to enhance the photocatalytic activity of Cu_2O for oxidative C-C bond formation, Appl. Catal. B- Environ. 213 (2017) 1–8.
[46] M. Li, H. Zhou, W. Yang, L. Chen, Z. Huang, N. Zhang, C. Fu, Y. Kuang, Co_9S_8 nanoparticles embedded in a N, S co-doped graphene-unzipped carbon nanotube composite as a high performance electrocatalyst for the hydrogen evolution reaction, J. Mater. Chem. A 5 (2017) 1014–1021.
[47] J. Zhang, H. Zhou, X.B. Liu, J. Zhang, T. Peng, J.L. Yang, Y.H. Huang, S.C. Mu, Keratin-derived S/N co-doped graphene-like nanobubble and nanosheet hybrids for highly efficient oxygen reduction, J. Mater. Chem. A 4 (2016) 15870–15879.
[48] H. Ren, X. Shi, J. Zhu, Y. Zhang, Y. Bi, L. Zhang, Facile synthesis of N-doped graphene aerogel and its application for organic solvent adsorption, J. Mater. Sci. 51 (2016) 6419–6427.
[49] J. Yu, J. Jin, B. Cheng, M. Jaroniec, A noble metal-free reduced graphene oxide–CdS nanorod composite for the enhanced visible-light photocatalytic reduction of CO2 to solar fuel, J. Mater. Chem. A 2 (2014) 3407.
[50] Y. Lei, C. Yang, J. Hou, F. Wang, S. Min, X. Ma, Z. Jin, J. Xu, G. Lu, K.-W. Huang, Strongly coupled CdS/graphene quantum dots nanohybrids for highly efficient photocatalytic hydrogen evolution: unraveling the essential roles of graphene quantum dots, Appl. Catal. B- Environ. 216 (2017) 59–69.
[51] M.-Q. Yang, C. Han, Y.-J. Xu, Insight into the effect of highly dispersed MoS_2 versus layer-structured MoS_2 on the photocorrosion and photoactivity of CdS in graphene–CdS–MoS_2 composites, J. Phys. Chem. C 119 (2015) 27234–27246.
[52] F.X. Xiao, J. Miao, B. Liu, Layer-by-layer self-assembly of CdS quantum dots/graphene nanosheets hybrid films for photoelectrochemical and photocatalytic applications, J. Am. Chem. Soc. 136 (2014) 1559–1569.
[53] S.B. Yang, L.J. Zhi, K. Tang, X.L. Feng, J. Maier, K. Mullen, Efficient synthesis of

heteroatom (N or S)-doped graphene based on ultrathin graphene oxide-porous silica sheets for oxygen reduction reactions, Adv. Funct. Mater. 22 (2012) 3634–3640.
[54] A. Pendashteh, J. Palma, M. Anderson, R. Marcilla, $NiCoMnO_4$ nanoparticles on N-doped graphene: highly efficient bifunctional electrocatalyst for oxygen reduction/evolution reactions, Appl. Catal. B- Environ. 201 (2017) 241–252.
[55] S. Dou, A.L. Shen, Z.L. Ma, J.H. Wu, L. Tao, S.Y. Wang, N-, P- and S-tridoped graphene as metal-free electrocatalyst for oxygen reduction reaction, J. Electroanal. Chem. 753 (2015) 21–27.
[56] X.B. Wu, Z.Y. Xie, M. Sun, T. Lei, Z.M. Zuo, X.M. Xie, Y.L. Liang, Q.Z. Huang, Edge-rich and (N, S)-doped 3D porous graphene as an efficient metal-free electrocatalyst for the oxygen reduction reaction, RSC Adv. 6 (2016) 90384–90387.
[57] X. Wang, G. Li, M.H. Seo, F.M. Hassan, M.A. Hoque, Z. Chen, Sulfur atoms bridging few-layered MoS_2 with S-doped graphene enable highly robust anode for lithium-ion batteries, Adv. Energy. Mater. 5 (2015) 1501106.
[58] Y. Tian, Z. Wei, X. Wang, S. Peng, X. Zhang, W.-M. Liu, Plasma-etched, S-doped graphene for effective hydrogen evolution reaction, Int. J. Hydrogen Energy 42 (2017) 4184–4192.
[59] S. Zhang, L. Wang, Y. Zeng, Y. Xu, Y. Tang, S. Luo, Y. Liu, C. Liu, CdS-nanoparticles-decorated perpendicular hybrid of MoS_2 and N-doped graphene nanosheets for omnidirectional enhancement of photocatalytic hydrogen evolution, ChemCatChem 8 (2016) 2557–2564.
[60] L.K. Putri, W.J. Ong, W.S. Chang, S.P. Chai, Heteroatom doped graphene in photocatalysis: a review, Appl. Surf. Sci. 358 (2015) 2–14.
[61] Z.K. Yue, A.J. Liu, C.Y. Zhang, J. Huang, M.S. Zhu, Y.K. Du, P. Yang, Noble-metal-free hetero-structural CdS/Nb_2O_5/N-doped-graphene ternary photocatalytic system as visible-light-driven photocatalyst for hydrogen evolution, Appl. Catal. B-Environ. 201 (2017) 202–210.
[62] X. Yu, R. Du, B. Li, Y. Zhang, H. Liu, J. Qu, X. An, Biomolecule-assisted self-assembly of CdS/MoS_2/graphene hollow spheres as high-efficiency photocatalysts for hydrogen evolution without noble metals, Appl. Catal. B- Environ. 182 (2016) 504–512.
[63] X. Xu, G. Xu, Electrochemical impedance spectra of CdSe quantume dots sensitized nanocrystalline TiO_2 solar cells, Sci. Chin. Chem. 54 (2011) 205–210.
[64] D. Lang, T. Shen, Q. Xiang, Roles of MoS_2 and graphene as cocatalysts in the enhanced visible-light photocatalytic H_2 production activity of multiarmed CdS nanorods, ChemCatChem 7 (2015) 943–951.
[65] T.H. Yu, W.Y. Cheng, K.J. Chao, S.Y. Lu, $ZnFe_2O_4$ decorated CdS nanorods as a highly efficient, visible light responsive, photochemically stable, magnetically recyclable photocatalyst for hydrogen generation, Nanoscale 5 (2013) 7356–7360.
[66] Q. Zhang, P. Chen, M. Zhuo, F. Wang, Y. Su, T. Chen, K. Yao, Z. Cai, W. Lv, G. Liu, Degradation of indometacin by simulated sunlight activated CDs-loaded $BiPO_4$ photocatalyst: roles of oxidative species, Appl. Catal. B- Environ. 221 (2018) 129–139.
[67] F.Y. Pei, S.G. Xu, W. Zuo, Z.R. Zhang, Y.L. Liu, S.K. Cao, Effective improvement of photocatalytic hydrogen evolution via a facile in-situ solvothermal N-doping strategy in N-TiO_2/N-graphene nanocomposite, Int. J. Hydrogen Energy 39 (2014) 6845–6852.
[68] S.-D. Jiang, G. Tang, Y.-F. Ma, Y. Hu, L. Song, Synthesis of nitrogen-doped graphene-ZnS quantum dots composites with highly efficient visible light photodegradation, Mater. Chem. Phys. 151 (2015) 34–42.
[69] M.E. Khan, M.M. Khan, M.H. Cho, CdS-graphene nanocomposite for efficient visible-light-driven photocatalytic and photoelectrochemical applications, J. Colloid Interface Sci. 482 (2016) 221–232.
[70] E. Gao, W. Wang, M. Shang, J. Xu, Synthesis and enhanced photocatalytic performance of graphene-Bi_2WO_6 composite, Phys. Chem. Chem. Phys. 13 (2011) 2887–2893.
[71] Q. Xiang, J. Yu, M. Jaroniec, Graphene-based semiconductor photocatalysts, Chem. Soc. Rev. 41 (2012) 782–796.
[72] I. Vamvasakis, A. Trapali, J. Miao, B. Liu, G.S. Armatas, Enhanced visible-light photocatalytic hydrogen production activity of three-dimensional mesoporous p-CuS/n-CdS nanocrystal assemblies, Inorg. Chem. Front. 4 (2017) 433–441.
[73] J. Zhang, Z. Zhu, X. Feng, Construction of two-dimensional MoS(2)/CdS p-n nanohybrids for highly efficient photocatalytic hydrogen evolution, Chemistry 20 (2014) 10632–10635.
[74] J. Liu, J. Ke, D. Li, H. Sun, P. Liang, X. Duan, W. Tian, M.O. Tade, S. Liu, S. Wang, Oxygen vacancies in shape controlled Cu_2O/reduced graphene oxide/In_2O_3 hybrid for promoted photocatalytic water oxidation and degradation of environmental pollutants, ACS Appl. Mater. Interfaces 9 (2017) 11678–11688.
[75] K. Chang, M. Li, T. Wang, S. Ouyang, P. Li, L. Liu, J. Ye, Drastic layer-number-dependent activity enhancement in photocatalytic H_2 evolution over nMoS_2/CdS ($n \geq 1$) under visible light, Adv. Energy Mater. 5 (2015) 1402279.
[76] X. Duan, Z. Ao, H. Sun, S. Indrawirawan, Y. Wang, J. Kang, F. Liang, Z.H. Zhu, S. Wang, Nitrogen-doped graphene for generation and evolution of reactive radicals by metal-free catalysis, ACS Appl. Mater. Interfaces 7 (2015) 4169–4178.
[77] L.K. Putri, B.-J. Ng, W.-J. Ong, H.W. Lee, W.S. Chang, S.-P. Chai, Heteroatom nitrogen- and boron-doping as a facile strategy to improve photocatalytic activity of standalone reduced graphene oxide in hydrogen evolution, ACS Appl. Mater. Interfaces 9 (2017) 4558–4569.
[78] X.-K. Kong, C.-L. Chen, Q.-W. Chen, Doped graphene for metal-free catalysis, Chem. Soc. Rev. 43 (2014) 2841–2857.